Calibration of a Fast-Neutron Time-of-Flight System

Javier Morales

Thesis submitted for the degree of Master of Science
Project presented: December 2020

Supervised by
Kevin Fissum

Department of Physics
Division of Nuclear Physics
December 2020

Abstract

Future experiments with thermal neutrons at neutron facilities may encounter fast neutrons as sources of background. Understanding fast neutron behavior on an event-by-event basis in a detector is important for these complementary thermal neutron experiments. One way to study fast neutron events is by performing a time-of-flight measurement. In this thesis, a calibration of a neutron time-of-flight spectrum using emissions from an Actinide/Beryllium source was performed. Neutron kinetic energies were determined using the neutron-tagging technique, where each fast neutron was correlated to a gamma-ray from the decay of the first excited state of Carbon. The results indicate the technique functions as expected.

Contents

List of Figures

List of Tables

List of Abbreviations

- **ESS** European Spallation Source
- **Linac** Linear Accelerator
- **ToF** Time-of-Flight
- **YAP** Yttrium Aluminum Perovskite
- **PMT** Photomultiplier Tube
- **CFD** Constant-Fraction Discriminator
- **STF** Source-Testing Facility
- **ADC** Analog-to-Digital Converter
- **FWHM** Full-Width-at-Half-Maximum

Acknowledgements

First and foremost, a deep and sincere gratitude to my supervisor Kevin Fissum for all his patience, flexibility, guidance, and genuine interest in seeing this work succeed. Sincere appreciation is also extended to members (old and current) of the Lund University Neutronics Group, in particular Fransesco Messi, Rasmus Kjær Høier, Nicholai Mauritzson, and Emil Rofors for their willingness to help and for creating a welcoming environment. Ignacio Prado, Daniel Passeltiner, Juan José Morales, Lisa Rämich, Maitane Muñoz, Paul André, and Philipp Strumer for their tips and assistance, however large or small, in computer coding was greatly appreciated; so was Alex Kalee's and Timea Vitos' help in clarifying concepts in statistics. I also want to thank the Bates College Physics Department (2014 - 2016), specially professors Travis Gould and Eric Wollman for their previous teaching. Finally, but most essential of all, thank you to my family and previous sponsors for making this education possible.

Chapter 1 | Introduction

1.1 Motivation

Neutrons can be used to probe matter [1]. The European Spallation Source (ESS) [2] being built in Lund, Sweden will be the most powerful neutron facility in the world. ESS will accelerate protons with a linear accelerator (linac) and collide them with a tungsten target. This process of neutron production is known as spallation. The neutrons produced via spallation have an energy range of $10^1 - 10^2$ MeV. The resulting spallation neutrons are slowed down with materials in a process known as thermalization. These thermal neutrons with an energy of 25 meV (the most probable energy for neutrons at room temperature) are of particular interest as an atomic probe due to their wavelength of $\sim$ 1 Å. This makes them useful tools for the study of matter on an atomic scale. The thermal neutrons are guided in beamlines to experimental halls. In these halls, the thermal neutrons interact with samples via scattering to reveal information about the sample. Specialized detectors are needed to study the scattered neutrons. Higher energy neutrons are inevitable sources of background radiation in spallation sources. This reduces the signal-to-noise ratio of thermal neutron detectors. It is important to understand these higher energy neutrons on an event-by-event basis. One method of measuring neutron energies is through a technique called Time-of-Flight (ToF). This thesis involved calibrating a high-energy neutron ToF system with a well known radioactive source on an event-by-event basis.

1.2 Chargeless Particles

1.2.1 Neutrons

Along with the proton, the neutron is one of two particles that make up the atomic nucleus. Together, these two particles are referred to as nucleons. While the proton has a positive electrical charge q = 1.6×10^{-19} C, the neutron is electrically neutral. The neutron, with a mass of $939.6 \pm (5.8 \times 10^{-7}) \frac{\text{MeV}}{c^2}$, is slightly heavier than the proton at $938.3 \pm (5.8 \times 10^{-7}) \frac{\text{MeV}}{c^2}$ [3], where c is the speed of light. Neutrons that are not bound in an atomic nucleus are referred to as free neutrons and have a lifetime of approximately 10 minutes, after which they undergo beta decay.

Lacking an electric charge, free neutrons are unaffected by the Coulomb force and interact with other nuclei via the strong interaction. The speed of free neutrons, and hence their kinetic energy, determines their probability of interaction with other nuclei. This probability of interaction is referred to as a cross section. It is therefore useful to classify neutrons according to their energy.

Thermal neutrons are defined to have an energy of 25 meV. Cold neutrons have energies lower than 25 meV and fast neutrons have energies in the MeV range. Exact definitions of

fast neutrons vary depending on the author. In this work, fast neutrons are defined as those with energies from 0.1 - 10 MeV.

Neutron-nucleus interactions are dependent on the incoming neutron energy and the target nucleus. These interactions include scattering and absorption. Scattering can be either elastic or inelastic. In the latter case, incident neutron kinetic energy is lost to the nuclear excitation. This is most likely to occur at energies in the MeV range. In elastic scattering, the kinetic energy of the incident neutron is conserved. Nuclear absorption occurs when a neutron is absorbed by the nucleus resulting in a new isotope. The slower the neutron, the more likely it is to be captured by a nucleus due to longer interaction time. Neutron absorption is more likely to occur at lower energies, as the cross section scales as $\frac{1}{v_n}$ where v_n is the neutron speed. The new isotope may then decay and emit ionizing radiation. Examples of these three types of neutron-nuclei interaction are depicted in Figure 1.1.

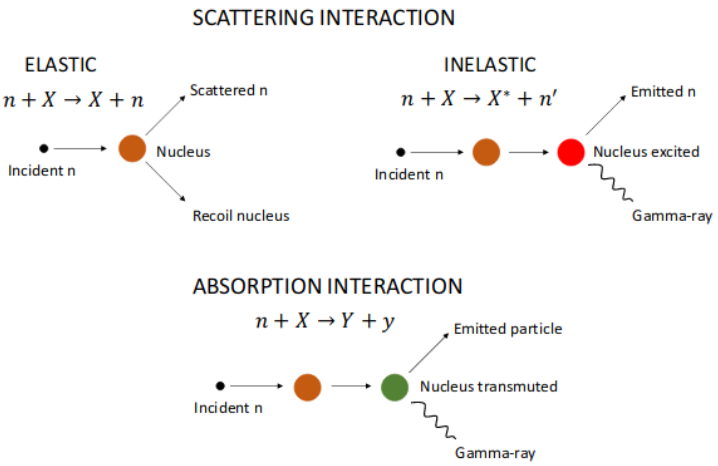

Figure 1.1: Neutron-nucleus interactions. Neutrons interact via elastic scattering (top left), inelastic scattering (top right), and nuclear absorption (bottom). Image taken from [4].

1.2.2 Photons

The photon is the elementary exchange particle for the electromagnetic force. Like neutrons, photons have no electric charge. Unlike neutrons, photons are massless. Photons with the highest energies have the shortest wavelengths. Gamma-rays have energies in the range of keV to MeV and originate from the nucleus.

Photons of different energies interact differently with matter. At energies in the eV range, photons interact with atomic electrons mainly via the photoelectric effect. Here, the electron absorbs the incoming photon and is ejected from the atom with a kinetic energy equal to the difference between the energy of the photon and the binding energy of the electron. In the range between $0.1 - 5$ MeV, photons interact with matter mainly via Compton scattering. Here, the photon is scattered by a bound electron, resulting in an energy transfer to the electron. The recoiling electron is either excited or freed. The scattered photon continues

to interact with the material. At energies above 5 MeV, pair production dominates. Here, photons with a minimum energy of twice the rest mass of the electron (1.022 MeV/c^2) are converted into electron-positron pairs in the vicinity of a nucleus [5]. These two particles continue to interact within the material until the positron stops and is annihilated with another electron, resulting in two additional photons with energies of 0.511 MeV [6]. The two newly created photons may then interact further within the material or escape the material entirely without further interaction. The escaping gamma-rays lead to escape peaks in the gamma-ray spectrum. The photoelectric effect cross section varies as Z^2, the Compton scattering cross section scales linearly with Z, and the pair production cross section varies as Z^5 [7]. Therefore, materials with higher Z are usually chosen for gamma-ray detection.

1.3 Neutron/Gamma-Ray Sources

Neutrons and gamma rays are produced naturally through the spontaneous fission of certain elements and through nuclear reactions following radioactive decay. Actinide/Beryllium sources are regularly used as sources of free neutrons. Actinides are elements with atomic numbers 89 - 103. ^{9}Be is a stable isotope which has an atomic number of $Z = 4$. In these types of sources, an Actinide isotope emits a ^{4}He nucleus via α-decay. For example,

$$^{238}\mathrm{Pu} \rightarrow \ ^{234}\mathrm{U}^{(*)} + \alpha + Q, \tag{1.1}$$

where Q is the mass-energy equivalence difference ($Q = \Delta mc^2$) between the parent (^{238}Pu) and daughter (^{234}U) nuclides and the α-particle. More than 60% of the time [8], the ^{234}U is left in a variety of excited states denoted by $^{(*)}$. $^{234}\mathrm{U}^{(*)}$ relaxes to its ground state via the emission of one or more gamma-rays with various energies

$$^{234}\mathrm{U}^{(*)} \rightarrow \ ^{234}\mathrm{U} + \Sigma\gamma. \tag{1.2}$$

Gamma-rays produced in this process are referred to as a gamma cascade and are denoted by $\Sigma\gamma$ in Eq (1.2).

The α-particles from the decay of ^{238}Pu can be captured by a ^{9}Be nucleus resulting in the reaction products ^{12}C and a fast neutron

$$\alpha + {}^9\mathrm{Be} \rightarrow \ ^{12}\mathrm{C}^{(*)} + n + Q. \tag{1.3}$$

Approximately 55% of the time [9], the recoiling ^{12}C isotope is produced in its first excited state $^{12}\mathrm{C}^{(*)}$. The $^{12}\mathrm{C}^{(*)}$ promptly relaxes to its ground state via the emission of a 4.44 MeV gamma-ray

$$^{12}\mathrm{C}^{(*)} \rightarrow \ ^{12}\mathrm{C} + \gamma(4.44\ \mathrm{MeV}). \tag{1.4}$$

Figure 1.2 shows an energy spectrum of fast neutrons emitted from a PuBe source. The emitted neutrons extend up to 11 MeV. Theoretically, the range includes energies between 0 and 1 MeV. Experimentally, however, neutrons with less than 1 MeV did not deposit sufficient energy to be detected by the particular detector setup.

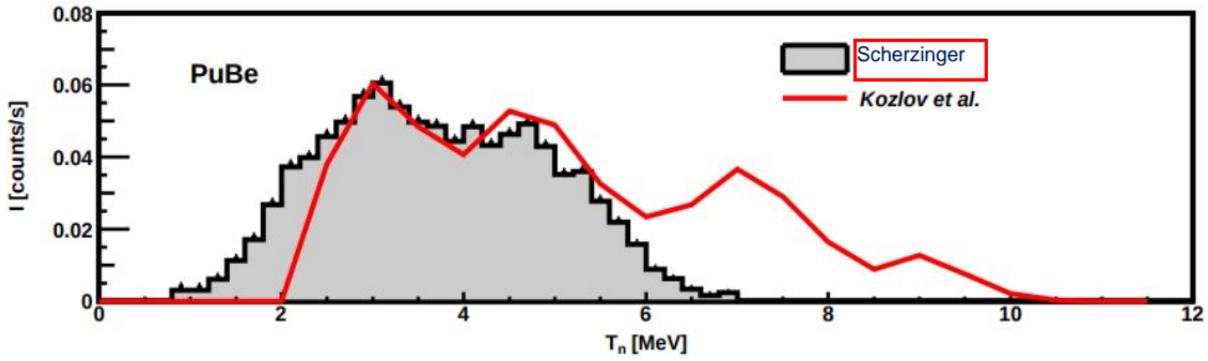

Figure 1.2: PuBe neutron energy spectra. Energy spectra from measurements of tagged (grey) and untagged (red) neutrons. Image taken from [10].

When $^{12}C^{(*)}$ de-excites with the emission of a 4.44 MeV photon, the free neutron produced has a maximum energy E_n of

$$E_n \sim 6.6 \text{ MeV}. \tag{1.5}$$

The value of E_n is obtained from the Q values. This joint emission of a 4.44 MeV gamma-ray and a free neutron with an energy up to $\sim$ 6.6 MeV can be exploited to "tag" the neutron. The details of this tagging technique are explained in Sect. 1.6. Figure 1.3 shows the energy spectrum of gamma-rays from the PuBe source. The 2.61 MeV peak is from the de-excitation of $^{208}Pb^{(*)}$ and is due to isotropic impurities in the source and room background. Table 1.1 summarizes expected emissions from the PuBe source.

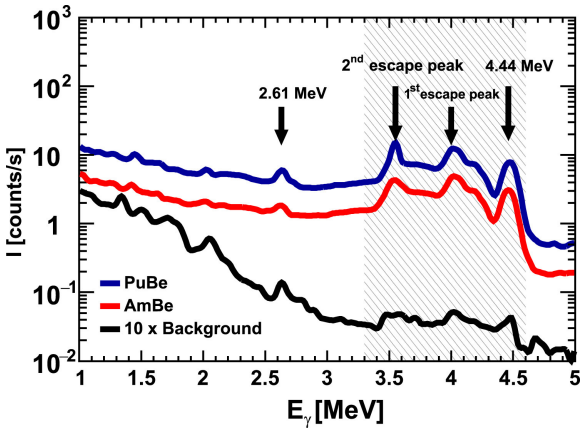

Figure 1.3: PuBe gamma-ray spectra. From the top: PuBe (blue), AmBe (red), background (black). The grey shaded region illustrates 4.44 MeV gamma-rays. Figure taken from [10].

Table 1.1: PuBe emissions summary.

Emission rate (neutrons/second)	2.66×10^6 [10]
Neutron MeV range (approximate)	1 - 11
Approximate neutron energy peaks (MeV)	3.5, 4.5
Primary gamma-ray energy peaks (MeV)	4.44

1.4 Scintillation Detectors

The lack of electric charge in the neutron means they cannot be detected directly. Instead, an intermediate step is needed in which neutrons induce nuclear reactions or scatter in matter and produce detectable ionizing radiation. Neutron detection thus depends on the partial or total transfer of the neutron energy to a target nucleus. Since neutron behavior is energy dependent, different methods exist to detect thermal and fast neutrons. Similarly, gamma-rays themselves are not observed directly due to their short wavelengths. Instead, their effect on matter is detected. Gamma-rays interact with atomic electrons, also imparting some or all of their energy.

1.4.1 Scintillators

Scintillators emit light when exposed to radiation. The scintillation light is produced by the relaxation of electron states excited by incident radiation, as in prompt fluorescence, phosphorescence, and delayed fluorescence. Materials which scintillate may be organic or inorganic in composition and can be in different states (solid, liquid, or gaseous). Certain features of scintillators make them effective detectors for irradiation experiments. Good scintillators require that a large portion of incident radiation is converted into prompt fluorescence [5]. When operated correctly, their light output can be proportional to the incoming radiation. A fast response time is important as it allows for the time difference between two succeeding events to be determined with greater precision. A fast recovery time is also important because the scintillator recovers quickly from radiation-induced excitation can thus handle a high count rate.

Organic Scintillators

Organic scintillators are useful for fast-neutron detection because they contain a high amount of ^{1}H atoms. They are also sensitive to gamma-rays. As explained earlier, fast neutrons interact with nuclei mainly by elastic scattering. During a neutron-nucleus collision, energy and momentum are transferred from the incoming neutron to the target nucleus. The lighter this nucleus, the higher the possible energy transfer from the incoming neutron. In a ^{1}H nucleus, the energy transfer can be up to 100%. This is due to the nearly equal masses of the proton and neutron. The resulting energy E_f of the recoil nucleus after the collision is described by

$$E_f = \frac{4A}{(1+A)^2}\cos^2(\theta)E_i, \tag{1.6}$$

where A is the mass of the target nucleus, θ is the scattering angle of the recoil nucleus with respect to the incident neutron in the center-of-momentum frame, and E_i is the initial neutron energy. The recoiling nucleus then deposits energy in the medium which leads to scintillation. Table 1.2 summarizes the maximum energy transfers between neutrons and a few light nuclei.

Table 1.2: Energy transfer from a neutron to various targets. Table from [5].

Target nucleus	A	$(E_f/Ei)_{max}$
^{1}H	1	1.000
^{2}H	2	0.889
^{3}He	3	0.750
^{4}He	4	0.640
^{12}C	12	0.284
^{16}O	16	0.221

Certain organic molecules have what is called a π-electron structure [5]. Valence electrons between molecules are loosely bound in these π-electron orbitals. Scintillation light is the result of these electrons de-exciting from a singlet (S = 0) or triplet (S = 1) state to the ground state. Additionally, atoms in molecules can vibrate resulting in vibrational states of the molecule. Figure 1.4 depicts an energy-level diagram for π-electron orbital. Note that scintillation photons are produced from the decays of S^* to S_0 and from T_0 to S^*. The internal degradation decays from S^{**} to S^* do not result in scintillation light.

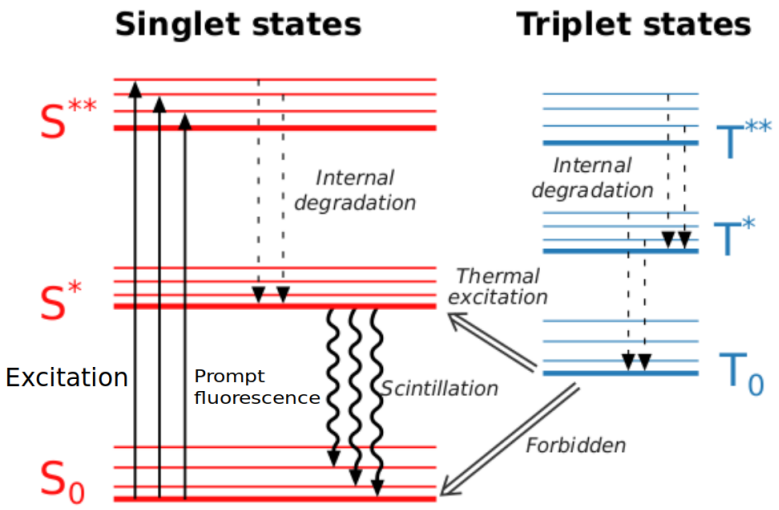

Figure 1.4: Scintillation process in organic scintillators. The singlet and triplet states are shown in red and blue, respectively. The thicker bottom lines of each state represent the energy levels and the thinner lines represent the associated molecular vibrational states. The wavy lines represent scintillation from prompt fluorescence. Figure adapted from [11], originally from [7].

Incident radiation generally interacts with several molecules and thus many states may be excited. For the singlets, the excited states S^{**} decaying to S^{*} do not emit scintillation light. Scintillation photons are the result of the subsequent, fast decay of S^{*} to S_0. For the triplets, T_0 may decay through a longer process first to S^{*} and then to S_0.

The organic liquid scintillator detector used in this thesis is an NE-213. As explained in [7], the NE-213 is the standard for neutron detection because of its efficiency and ability to distinguish between gamma-ray and neutron radiation. Some of its properties are highlighted in Table 1.3.

Table 1.3: Properties of the organic liquid scintillator NE-213 [12].

Property	Value
Density (g/cm^3)	0.873
Wavelength of maximum emission (nm)	425
Decay time (ns)	3
Refractive index	1.505
No. of H atoms/cm^3 ($\times 10^{22}$)	4.82
No. of c atoms/cm^3 ($\times 10^{22}$)	3.98
No. of electrons /cm^3 ($\times 10^{23}$)	2.27

Inorganic Scintillators

Inorganic scintillators are most often solids with a crystal lattice structure, usually doped with an activator. In inorganic scintillators, the excitation and scintillation processes happen between the valence and conduction bands. Inorganic crystal scintillators with higher atomic numbers and doped with activators are preferred for gamma-ray detection. This is due to their high light output and good energy resolution.

Electrons in the valence band are excited to the conduction band by the incident radiation. Due to the activator, energy states exist in the band gap which facilitate the transition from the states in the conduction band to the activator ground state, resulting in scintillation photons. This process is shown in Fig. 1.5.

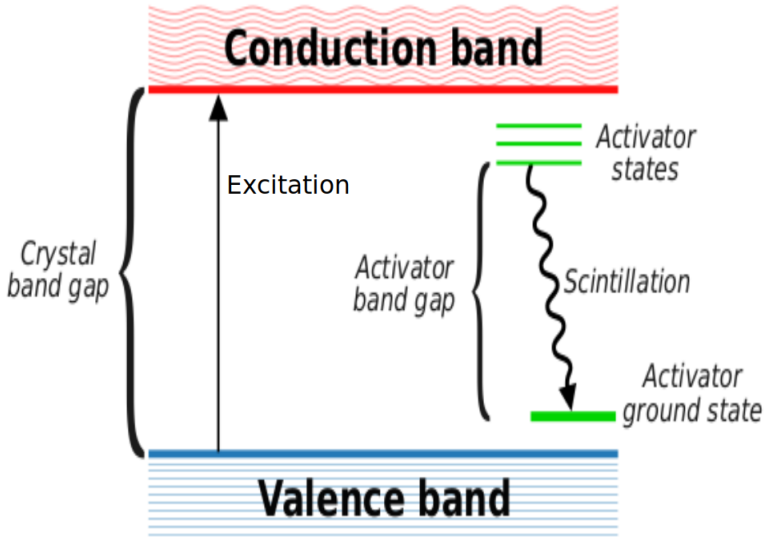

Figure 1.5: Scintillation process in inorganic scintillators. An electron excited from the valence band (in blue) to the conduction band (in red) decays via the activator states (in green) to the activator ground state, emitting scintillation (wavy line) in the process. Figure retrieved from [11].

The gamma-ray detector used in this thesis is an inorganic, Cerium-doped Yttrium Aluminum Perovskite crystal (YAP) scintillator. YAP is an efficient inorganic gamma-ray detector. With a $Z \approx 31$, YAP also has a fast rise time of $\sim$ 5 ns and a prompt decay time of $\sim$ 27 ns [10]. These quick processes allow for both fast timing of events and a high event count rate. The Cerium doping is to prevent the scintillation light from being re-absorbed by the scintillator itself. Some of the properties of the YAP are summarized in Table 1.4.

Table 1.4: Properties of the Cerium-doped YAP inorganic crystal scintillator [13].

Property	Value
Density (g/cm^3)	5.37
Wavelength of maximum emission (nm)	370
Decay time (ns)	25
Crystal structure	Rhombic
Index of refraction	1.95
Radiation length (cm)	2.7

1.4.2 Photomultiplier Tubes

Light produced via scintillation may be converted to an electrical signal via photomultiplier tubes (PMTs). Scintillators are often coupled with PMTs [7]. In a PMT, a photon interacts with the photocathode, creating a free electron due to the photoelectric effect. Since a single electron is difficult to detect, amplification is needed. High voltage is applied across the PMT, creating a potential difference between the photocathode and anode. The electric field guides the electrons towards a set of electron multipliers called dynodes. Electrons striking

the dynodes result in a secondary emission of electrons and an avalanche-like multiplication effect. The electron avalanche is then further guided towards the anode. If operated properly, this analog electron pulse created in the PMT may be proportional to the incident energy of the photon. A diagram of a PMT and its inner mechanism is presented in Fig. 1.6. The resulting analog signals take the form of current pulses.

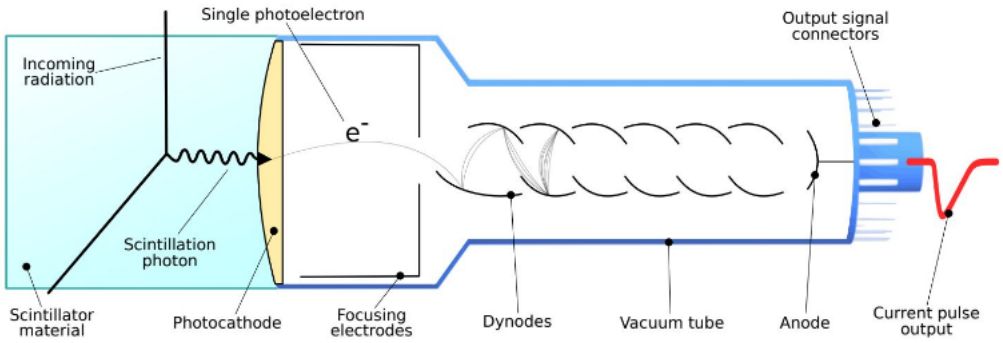

Figure 1.6: A scintillator detector coupled to a photomultiplier tube. The single photoelectron denoted by a gray curve is multiplied at each of the dynodes. The analog current pulse signal, depicted in red, is the resulting electrical signal. Image taken from [11].

1.5 Electronics

1.5.1 Digitizers

A digitizer, like a digital oscilloscope, is an electronic instrument which converts analog voltage signals into digital signals as function of time. Unlike a digital oscilloscope, which has a visual display, a digitizer prioritizes data transfer to a computer. To accurately reconstruct a digital version of an original signal, a digitizer needs proper sampling and slew rates. The input range of the digitizer corresponds to the maximum acceptable input voltage, or peak-to-peak voltage, V_{pp}. The resolution of the digitizer, given in bits, is V_{pp} divided into bins. The bandwidth of the digitizer is the frequency range for which the device can accurately reconstruct signals. The digitizer used in this thesis is the CAEN VX1751 waveform digitizer with eight Analog-to-Digital Converter (ADC) channels. A picture of the digitizer is shown in Fig. 1.7. It features a 1 GS/s sampling rate, a 500 MHz bandwidth, V_{pp} of 1 V, and 10-bit resolution [14]. The 10-bit resolution means the input range is divided into $2^{10} = 1,024$ bins, each with a size of 9.78×10^{-4} V. This digitizer is useful for measuring signals from fast organic and inorganic liquid scintillators [14].

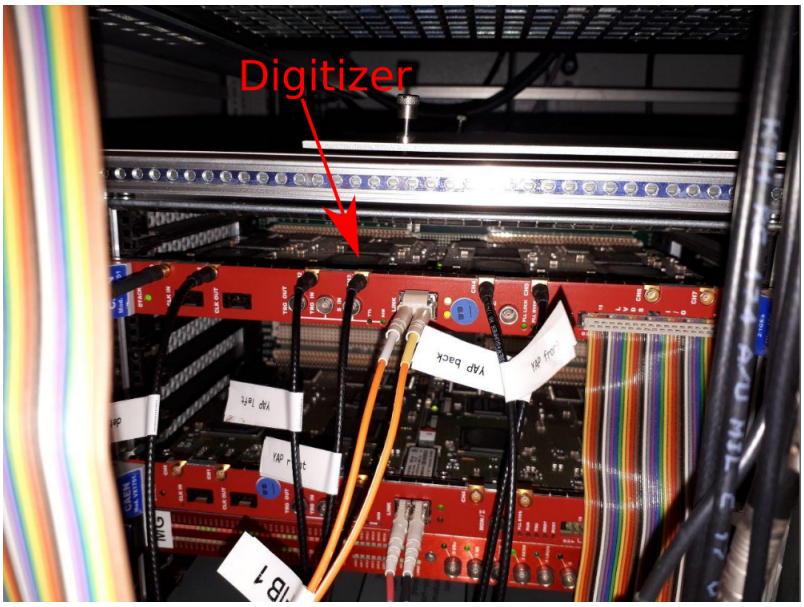

Figure 1.7: The CAEN VX1751 waveform digitizer. The digitizer is mounted in the top crate.

1.5.2 Constant-Fraction Discriminators

Precision time stamping of detector pulses is essential for accurate time measurements. Signals can be recorded using a threshold trigger. In this case, an electric signal that exceeds a predetermined, minimum amplitude known as a threshold is recorded as an event. However, if two similarly shaped signals of different amplitudes arrive at the same time they can be recorded with different time stamps, decreasing measurement accuracy. This is called the walk effect and is depicted in Figure 1.8. To eliminate the walk effect, software-based Constant-Fraction Discriminators (CFDs) are implemented to improve the timing of signals. Figure 1.9 depicts the principle of a CFD. A fixed fraction of the signal amplitude (70%) is set as trigger. In this way, the detector records an event when the amplitude of a signal exceeds 70% of its amplitude. To improve the accuracy of the time measurements, the same software CFD developed for [15] was employed.

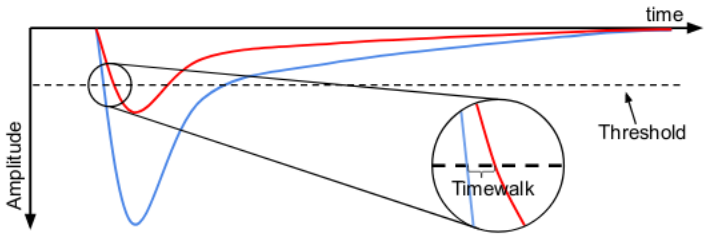

Figure 1.8: An illustration of the walk effect. The red and blue lines are signals of different amplitudes arriving at the same time. The encircled portion shows the walk effect. Image taken from [11].

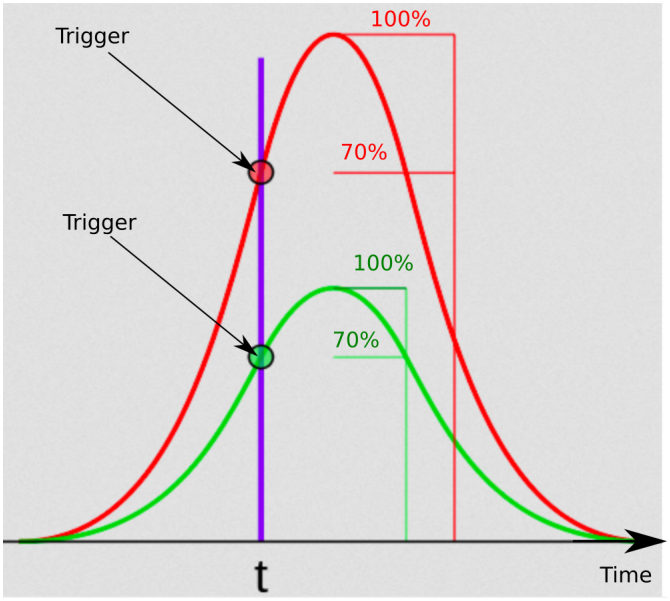

Figure 1.9: The principle of a constant-fraction discriminator. The green and red lines are signals of different amplitudes arriving at the same time. The purple line at point t shows the point at which both signals exceed 70% of their amplitude. Image adapted from [16].

1.5.3 Digital Time Stamps

The time stamping of the events is done by the digitizer itself. The digitizer passes the digitized signals associated with the registering channel together with a time stamp from the global clock. This clock, however, triggers on a threshold of the leading edge of a pulse which can lead to the walk effect. Thus, the software CFD from [15] was used to correct the time stamping.

1.6 Time-of-Flight

The time necessary for a particle to traverse a known distance is referred to as the time-of-flight (ToF) of the particle. The ToF method may be used to precisely measure neutron velocities. A sketch representing the timing of the signals of a ToF measurement is shown in Fig. 1.10.

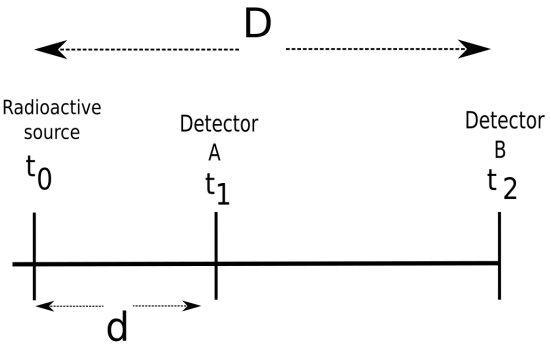

Figure 1.10: Start and stop signals for the time-of-flight measurement. The time t_0 is the time of emission of gamma-rays and the neutron from the source. t_1 is the time of a gamma-ray detected in Detector A and t_2 is the time of a gamma-ray detected in Detector B. The distance D is much larger than d.

When measuring the time difference between events detected in the gamma-ray detector (A) and the neutron-gamma ray detector (B), four important times are defined:

- t_0 is the time of gamma-rays and neutron emissions from the PuBe source
- t_1 is the time of a gamma-ray detected in the gamma-ray detector (A)
- t_2 is the time of a gamma-ray detected in the neutron-gamma ray detector (B)
- t_3 is the time of a neutron detected in the neutron-gamma ray detector (see Fig. 1.11).

Neutrons events in the YAP are neglected since it is insensitive to neutrons [10]. Note that the photons detected at t_2 and t_1 are predominantly from the gamma-ray cascade and not the de-excitation of ^{12}C.

Using the definitions of particle emission and detection times (t_0, t_1, t_2 and t_3), and the distances from the detectors to the radioactive source D and d, the following arises;

$$\begin{aligned} t_1 - t_0 &= \frac{d}{c} \\ t_2 - t_0 &= \frac{D}{c} \\ t_2 - t_1 &= \frac{D-d}{c} = \Delta t_{\gamma\gamma} \\ t_3 - t_0 &= \frac{D}{v_n} \\ t_3 - t_1 &= \Delta t_{n\gamma}, \end{aligned} \tag{1.7}$$

where c is the speed of light and v_n is the speed of a neutron. $\Delta t_{\gamma\gamma}$ is the time difference between a gamma-ray detected in the NE-213 and a gamma-ray detected in the YAP. $\Delta t_{n\gamma}$

is the time difference between a neutron detected in the NE-213 and a gamma-ray detected in the YAP. These times are shown in a timeline in Fig. 1.11. The time stamps t_1, t_2, t_3 are measured by the digitizers, while the distances D and d are fixed and pre-determined. The only unknown quantities are thus t_0 and v_n. Substituting in t_1 and t_3 for $\frac{D}{v_n}$ results in

$$\left(\frac{D}{v_n} + t_0\right) - \left(\frac{d}{c} + t_0\right) = \Delta t_{n\gamma}. \tag{1.8}$$

Adding the quantity $\frac{D}{c}$ to both sides yields

$$\frac{D}{v_n} - \frac{d}{c} + \frac{D}{c} = \Delta t_{n\gamma} + \frac{D}{c}. \tag{1.9}$$

Finally, substituting in the expression for $\Delta t_{\gamma\gamma}$ and rearranging results

$$v_n = \frac{D}{\Delta t_{n\gamma} - \Delta t_{\gamma\gamma} + \frac{D}{c}}. \tag{1.10}$$

Thus, the velocity of a neutron emitted from the PuBe source can be expressed in terms of the time differences between particle detection events and the distance between the PuBe and the NE-213. Furthermore, neutron ToFs can be measured with respect to the $\Delta t_{\gamma\gamma}$ events.

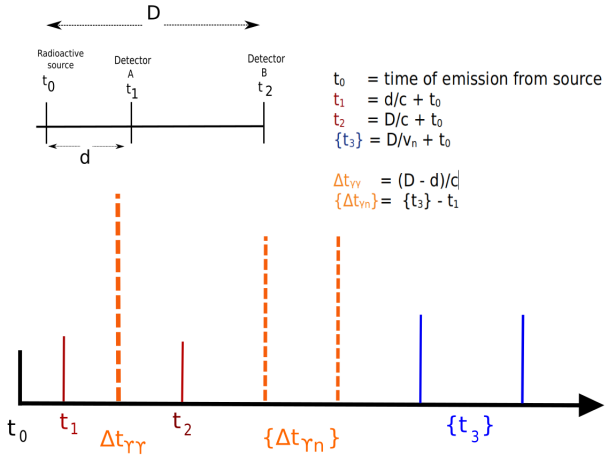

Figure 1.11: A time-of-flight event timeline. t_0 (black line) is the time of emissions of gamma-rays and neutrons from the source; t_1 (red line) is the time of a gamma-ray detected in the YAP; t_2 (red line) is the time of a gamma-ray detected in the NE-213; t_3 (blue lines) are the times of a neutrons detected in the NE-213. The dashed orange lines are time differences between detection events in the YAP and NE-213. The curly brackets {} signify a range of values, while the other events are fixed values.

The non-relativistic neutron velocities from Section 1.10 are then converted to energies via

$$T_n = \frac{m_n}{2} v_n^2, \tag{1.11}$$

where m_n and v_n are the mass and velocity of the neutron, respectively. Substituting for v_n yields

$$T_n = \frac{m_n}{2}\left(\frac{D}{\Delta t_{n\gamma} - \Delta t_{\gamma\gamma} + \frac{D}{c}}\right)^2. \tag{1.12}$$

Thus, the ToF method provides a way to measure neutron kinetic energies. A sketch of the expected ToF spectrum is shown in Figure 1.12. The $\Delta t_{\gamma\gamma}$ spike has many more counts than the $\Delta t_{\gamma n}$ structure because the large gamma-ray flux from the cascade is efficiently detected by the YAP close to the radioactive source. The broad distribution of the $\Delta t_{n\gamma}$ events is due to neutrons of varying energies emitted from the source. The background is caused by random coincidences between the neutron and gamma-ray detectors.

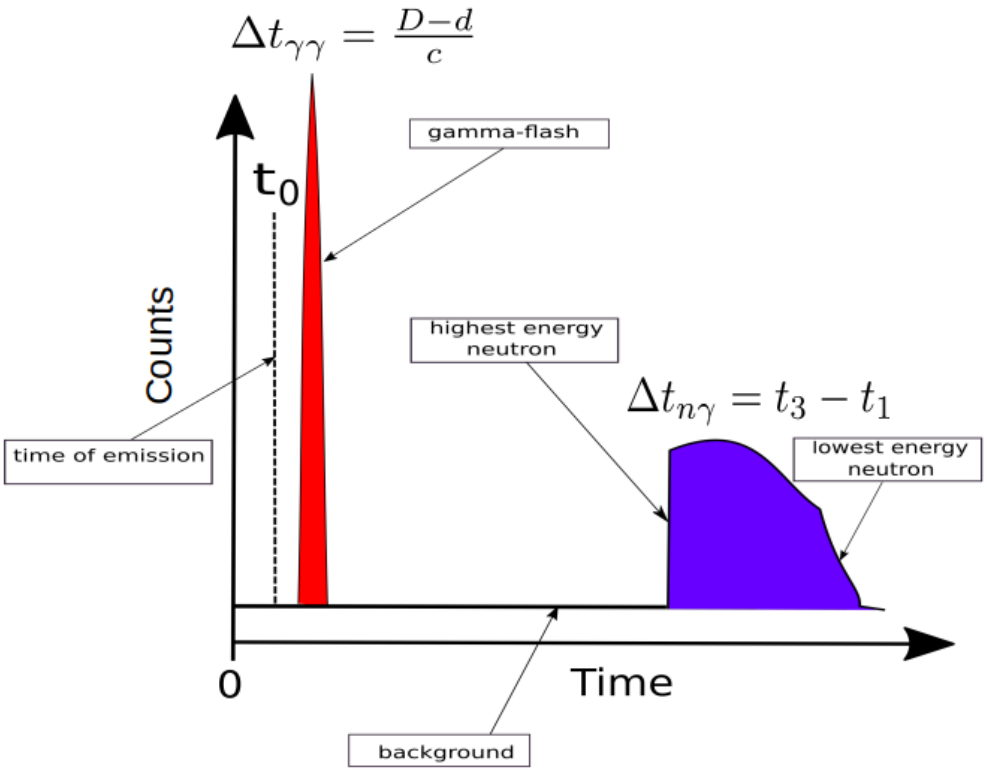

Figure 1.12: Expected structures in a ToF spectrum. The time of gamma-ray and neutron emissions from the source is denoted by t_0. The sharp spike comes from the $\Delta t_{\gamma\gamma}$ events (in red) while the shorter, broader structure further in the time scale are the $\Delta t_{\gamma n}$ events (in blue).

The classical kinetic energy formula is valid provided the kinetic energy of the particle is a small fraction of its rest mass. Since the most energetic neutrons that can be tagged have ~ 6.6 MeV of energy, classical laws still apply ($\frac{6.6}{939.6} \ll 1$). This can be confirmed by converting the maximum energy to speed. The resulting fraction $\frac{v_n}{c} \ll 1$.

Chapter 2 | Method

2.1 Source-Testing Facility

The Source-Testing Facility (STF) at Lund University [17] is equipped to perform neutron irradiation experiments. All the measurements in this thesis were carried out at the STF. A diagram depicting the STF is shown in Figure 2.1.

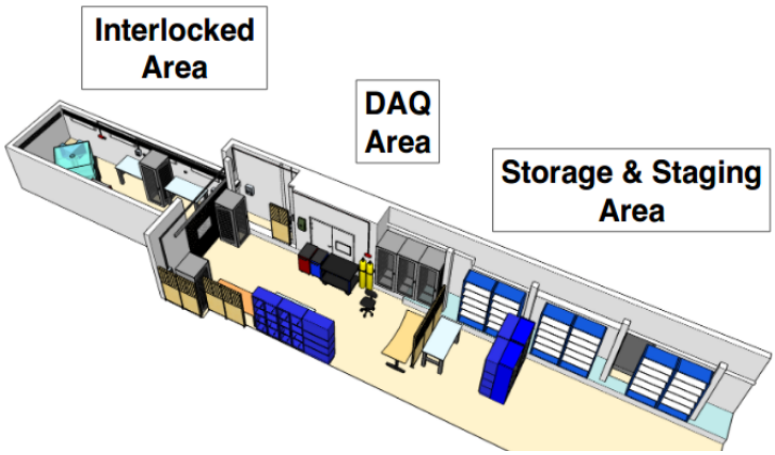

Figure 2.1: The Source-Testing Facility. The Interlocked Area is to the left, the Data Acquisition (DAQ) Area is in the middle, and the Storage and Staging Area is to the right. Image taken from [10].

The Interlocked Area houses the Aquarium and is used for measurements. The DAQ area houses the electronics. The Storage and Staging Area is a general space for equipment storage, including work stations.

2.2 The Aquarium

The STF has a PuBe source which can be placed at the center of a cubic container filled with pure, de-ionized water called the Aquarium. The source is placed in the center of the Aquarium, called the Inner Tank. This is used for user protection as the large volume of water shields users from dangerous levels of exposure. Up to four YAP detectors can be placed inside the Innter Tank as well, closely surrounding the source, for gamma-ray detection. There are four air-filled horizontal beam ports connecting the Inner Tank to the experimental hall to define beams for irradiation experiments. A sketch of the Aquarium is shown in Figure 2.2.

Radioactive sources within the Aquarium can be raised to a position in line with the central axis of the four horizontal beam ports so it is aligned vertically with externally

positioned detectors. It can also be lowered below the beam ports into a park position for maximal water shielding. Similarly, the YAP detectors can be placed at different heights surrounding the source so they are exposed to a gamma-ray flux without blocking the beams. The dimensions of the Aquarium are $(1.4 \times 1.4 \times 1.4)$ m^3.

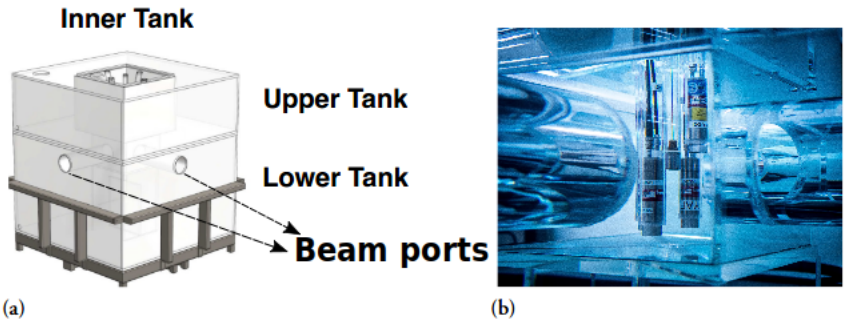

Figure 2.2: The Aquarium. (a) Two of the four beam ports are shown. (b) Shows a photo of the inner tank as seen from the outside. The source and four YAP detectors are visible. Image adapted from [10].

2.3 Actinide/Beryllium Source

The PuBe source used in this thesis has an emission rate of 2.99×10^6 neutrons per second [10]. It is encased in a cylindrical X.3 capsule made of steel which measures (31×22.4) mm^2. The source emits up to 11 MeV neutrons and a variety of lower energy gamma-rays in large quantities. Specific peaks in energies for neutrons and gamma rays can be seen in Fig. 1.2 and 1.3, respectively.

2.4 Detectors

2.4.1 NE-213

The NE-213 detector used in the measurements appears on the left in Fig. 2.3. The liquid scintillator is held in the cylindrical, aluminum cup measuring 6.0 cm in height and 9.4 cm in diameter. The NE-213 is coupled to a 3 inch PMT with lightguide and was operated at -2,080 V. The threshold of the detector was set at 24 mV.

2.4.2 YAP

The YAP detector used in the measurements appears on the right in Fig. 2.3. The crystal is cylindrical in shape and has a height of 2.5 cm and a 2.5 cm diameter. The YAP was coupled to a 2.5 cm PMT with lightguide operated at -755 V. The threshold of the detector was set at 24 mV.

Figure 2.3: The scintillator detectors used in this work. (left) The NE-213 liquid scintillator coupled to a PMT (the black tube). (right) The YAP crystal scintillator coupled to a PMT. Image taken from [10].

2.5 Experimental Setup

Figure 2.4 shows the experimental setup for this thesis. The NE-213 detector, sensitive to both neutrons and photons, is placed on a table in front of a beam port a distance $D =$ 1.306 m from the a PuBe source. The YAP detector, sensitive to gamma-rays, is held in a tube placed at a radial distance $d \sim$ 9.0 cm from the PuBe source out of the line-of-sight. Placing the YAP close to the source increases the detector solid angle. The source and the YAP were measured to be $\sim$ 8.3 cm apart.

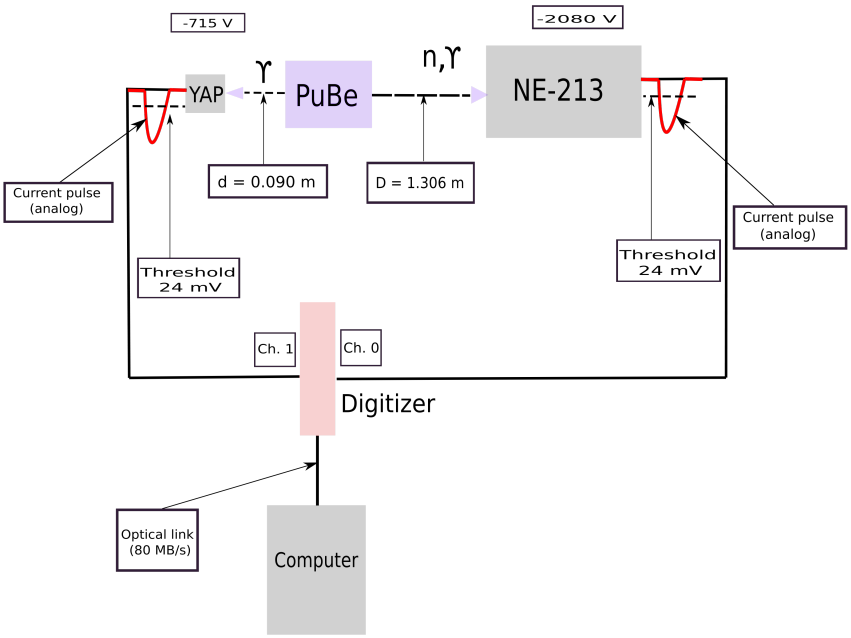

Figure 2.4: Experimental setup for the ToF measurement (not to scale). The YAP and NE-213 detectors are connected to different digitizer channels.

The PuBe source radiates isotropically, making it possible for both gamma-rays and neutrons to strike both detectors. The YAP, however, is mostly insensitive to neutrons and

neutron events in the YAP are not considered in these measurements. The combinations of events in the two detectors are summarized in Table 2.1. Note that γ_{cascade} is a collective label for the variety of gamma-rays from the gamma cascade and $\gamma_{^{12}\text{C}}$ are gamma-rays from the de-excitation of the $^{12}\text{C}^*$ nucleus. However, only the gamma-rays labeled $\gamma_{^{12}\text{C}}$ (the 4.44 MeV gamma-rays) can be used to tag the corresponding neutrons from the de-excitation of $^{12}\text{C}^*$. The gamma-flash is composed overwhelmingly of γ_{cascade} coincidence events.

Table 2.1: Coincidence combinations.

NE-213	**YAP**	**Used in ToF experiment**
n	$\gamma_{^{12}\text{C}}$	Yes
γ_{cascade}	γ_{cascade}	Yes
γ_{cascade}	$\gamma_{^{12}\text{C}}$	Yes
$\gamma_{^{12}\text{C}}$	γ_{cascade}	Yes
n	γ_{cascade}	No
n	n	No
γ_{cascade}	n	No
$\gamma_{^{12}\text{C}}$	n	No

2.5.1 Hardware

Both detectors are connected to different channels of the CAEN VX1751 waveform digitizer. The NE-213 is connected to channel 0 and the YAP is connected to channel 1. The digitizer itself is connected to a computer running CentOS 7.4 Linux distribution via an optical fiber cable with a speed of 80 Mb/s for data transfer.

2.5.2 Software

The digitizer runs on the WaveDump proprietary software also developed by CAEN [18]. A `bash` script was used to run the digitizer for data acquisition. The raw files produced by the digitizer are in `.h5` format and a set of `Python` scripts was used for data processing, mainly using the `Pandas` [19] library from `Python`.

2.5.3 Measurements

The data presented in this thesis are a result of 32 consecutive runs of 10 minutes each. The edge of the NE-213 detector was placed at a distance of 1.306 meters from center of the Aquarium at source height. The YAP was placed approximately 9 cm radially from the source at different a height. To prevent detector signals from overloading the V_{pp} of the digitizer, an attenuation of 16 dB was applied. Lead shielding was placed around the NE-213 to reduce background signals. Signals in the NE-213 were the trigger to start the ToF measurement. It is unknown exactly where the scintillation events occur within the scintillator, so the middle of the scintillator is chosen as an estimate.

Chapter 3 | Results

3.1 Time Calibration

The measured ToF spectra must be calibrated from digitizer channel units into seconds. This is achieved by shifting the rising edge of the gamma-flash from its initial position to 0 so that it is centered as expected at 4.16 ns based on the measurements of D and d. The left panel of Fig. 3.1 shows an uncalibrated ToF spectrum. When plotting the time differences between particle detection events, the $\Delta t_{\gamma\gamma}$ peak is expected as a narrow distribution centered around 4.16 ns. This expected value comes from the measurements for D and d. In contrast, the neutron events are expected within an approximate range of 38 - 96 ns due to their varying speeds. These values correspond to the maximum ($\sim$ 6.6 MeV) and minimum ($\sim$ 1 MeV) neutron energies used for tagging as explained in Sect. 1.2. A sketch of the positions of the center of the $\Delta t_{\gamma\gamma}$ events and neutron flight-time range is depicted in the right panel of Fig. 3.1.

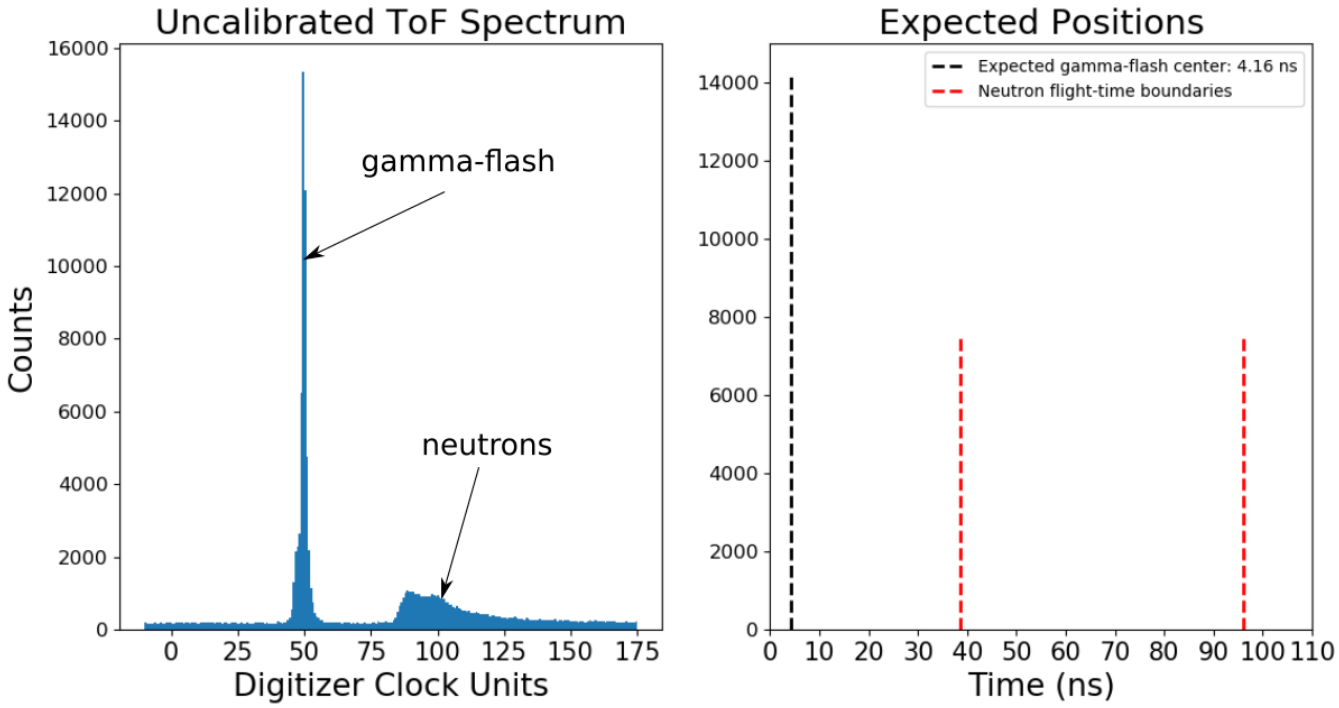

Figure 3.1: Uncalibrated versus expected ToF positions. (left) Uncalibrated ToF spectrum. (right) Expected position of the gamma-flash based on distance measurements and the slowest and fastest neutron flight-times indicated by the black and orange dashed lines, respectively.

The gamma-flash is a distribution of events and has an average value at the center of the distribution. A Gaussian function is used to approximate the gamma-flash distribution. Thus, the mean of the gamma-flash is equal to $\Delta t_{\gamma\gamma}$. A ToF spectrum was produced for each of the 32 runs to analyze them individually. Gaussian fits were applied to each gamma-flash distribution to obtain an experimental value of $\Delta t_{\gamma\gamma}$ as a function of run number. A sample spectrum with its corresponding Gaussian function fit is shown on the left plot in Fig. 3.2. Data from the detectors are shown in blue and the Gaussian curve fit is shown in orange. The constant background is given by p_0 and χ^2_r is the χ^2 value per degree-of-freedom for the fit. The value of p_0 is an average of histogram bin heights over the ranges 12 to 32 ns.

The right plot in Fig. 3.2 shows a scatter plot of all gamma-flash centers μ using the error in μ (σ_μ) and $\sigma/10$ as two uncertainties for comparison. Note the y-axis spans a single ns duration from 3.5 to 4.5 ns. The line of best fit was calculated using the least-squares approach. The value obtained was cross-referenced with the one from the `Python` library `SciPy` and found to be the same. The Gaussian $\sigma/10$ is a larger error margin than σ_μ. The best fit line misses nine data points including their $\sigma/10$ uncertainty margin. This corresponds to 28% of the data. This is an acceptable margin since 68% of data points should be found within a width of $\mu \pm \sigma$ in a Gaussian distribution. Table 3.1 below (split into runs 1 - 17 and runs 18 - 32) collects all 32 gamma-flash μ values and their associated uncertainties for each run.

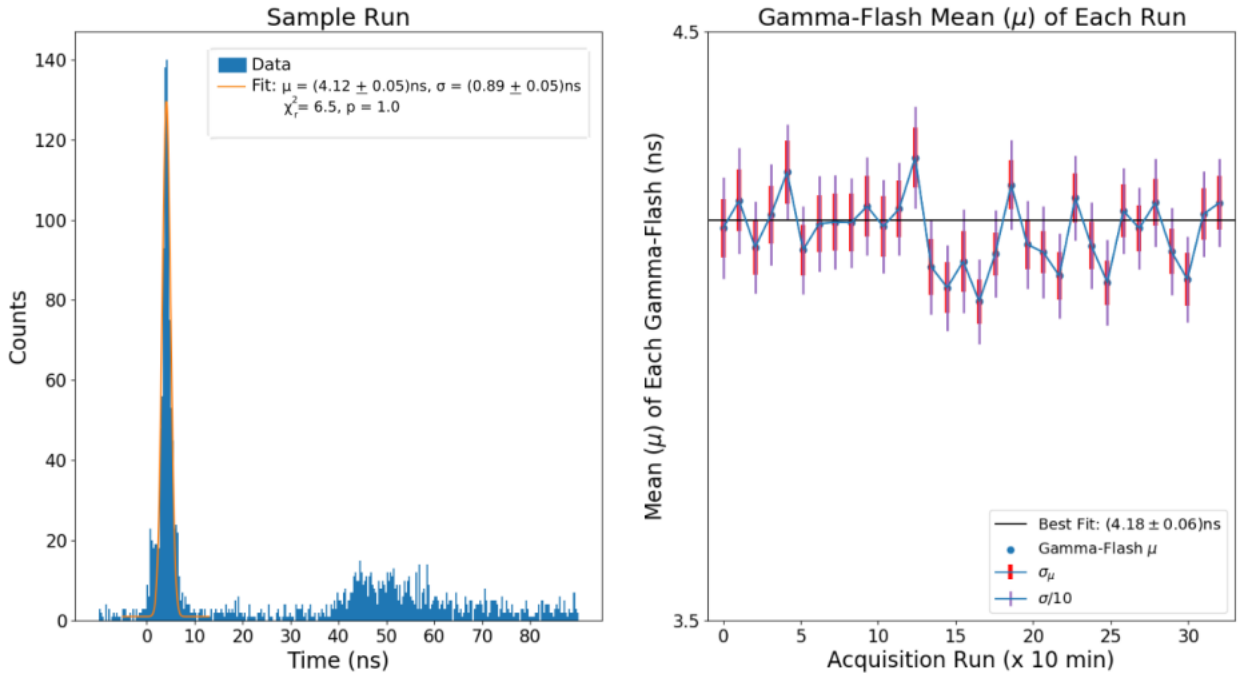

Figure 3.2: Sample run and gamma-flash means. (left) A ToF spectrum produced from one of the 32 acquisition runs. Data from the detectors is shown in blue and the Gaussian curve fit is shown in orange. (right) Collection of the gamma-flash centers (μ of the Gaussian fitted function) for all acquisition runs (blue dots). The line of best fit is shown in black. Note the y-axis starts goes from 3.5 - 4.5 ns.

Table 3.1: Gamma-flash position

Run	μ (ns)	σ_μ (ns)	$\sigma/10$ (ns)
1	4.17	0.04	0.09
3	4.21	0.04	0.08
4	4.13	0.04	0.09
5	4.19	0.04	0.08
6	4.26	0.04	0.08
7	4.13	0.04	0.08
8	4.17	0.04	0.08
9	4.18	0.04	0.08
10	4.18	0.04	0.08
11	4.20	0.04	0.08
12	4.17	0.04	0.08
13	4.20	0.04	0.09
14	4.29	0.04	0.08
15	4.10	0.04	0.07
16	4.07	0.04	0.09
17	4.11	0.03	0.07

Run	μ (ns)	σ_μ (ns)	$\sigma/10$ (ns)
18	4.04	0.03	0.08
19	4.12	0.03	0.08
20	4.24	0.03	0.07
21	4.10	0.03	0.08
22	4.07	0.03	0.07
23	4.11	0.03	0.07
24	4.04	0.04	0.07
25	4.12	0.04	0.07
26	4.07	0.03	0.07
27	4.20	0.03	0.07
28	4.17	0.03	0.07
29	4.21	0.03	0.07
30	4.13	0.03	0.07
31	4.08	0.03	0.07
32	4.19	0.04	0.07

3.2 Time-of-Flight

The entire ToF spectrum is shown in Fig. 3.3. The $\Delta t_{\gamma\gamma}$ events result in a narrow distribution with a sharp peak centered at (4.18 ± 0.06) ns as shown by the solid black line. The dashed black line centered at 4.16 ns is the predicted center of the gamma-flash distribution based on the measurements for D and d. The discrepancy of 0.02 ns between the expected central position of the gamma-flash and the experimental central position falls within the ± 0.06 ns uncertainty. Also note the highlighted range (in red) for the gamma-flash with bounds $(\mu \pm 3\sigma)$ which covers 99% of the gamma-flash distribution. The range of neutron flight times is as expected. The width of the gamma-flash is mainly due to the resolution of the NE-213 due to its larger volume compared to that of the YAP. A reliable approximation for the width of the gamma-flash is the full width at half maximum (FWHM) of the Gaussian fit which is 1.73 ns. An additional factor contributing to the width may be resolution and sampling rate of the digitizer and the CFD algorithm [15].

$\Delta t_{n\gamma}$ events result in a broadly distributed structure. The 38 ns lower bound of the $\Delta t_{n\gamma}$ distribution corresponds to the most energetic neutrons, while the 96 ns upper bound corresponds to the least energetic. Both peaks are plotted over a background representing random particle coincidences between the YAP and the NE-213 detectors over a 320 minute measurement span.

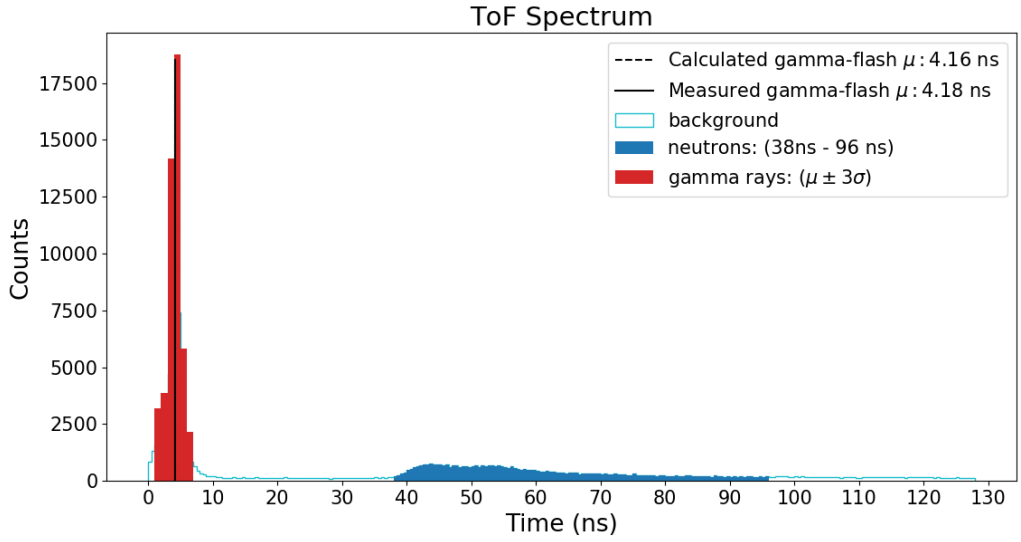

Figure 3.3: ToF distribution from PuBe. The gamma-flash is highlighted in red and the neutrons are highlighted in blue. Neutron events have a range from 38 ns to 96 ns. The background between the gamma-flash distribution and the neutron events are random coincidences.

3.3 Neutron Energies

The value of $\Delta t_{\gamma\gamma} = 4.16$ ns has an associated uncertainty ± 0.01 ns calculated by propagation of error using the expressions for t_1 and t_2 from Eq. 1.7. Increasing the gamma-flash implies longer flight times for both gamma-rays and neutrons due to longer distances. Furthermore, the kinetic energy expression derived earlier has an inverse squared dependence on $\Delta t_{\gamma\gamma}$. Changing the location of the gamma-flash by ± 0.01 ns does not affect the neutron energies significantly. The relationship between energies and ToF can be seen in Fig. 3.4.

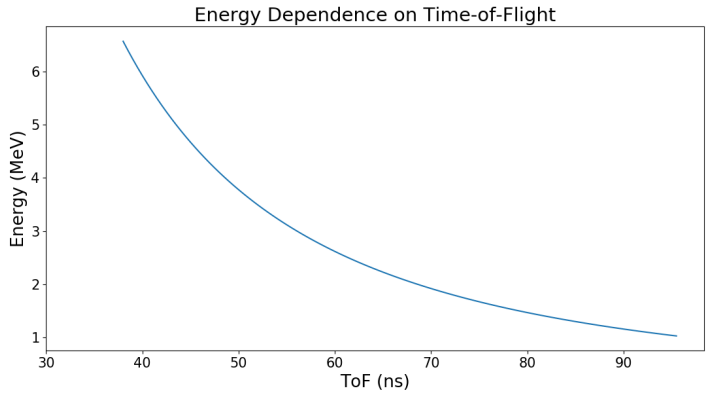

Figure 3.4: Neutron energy dependence on time-of-flight. The blue line shows an exponential decay in energies as ToF increases.

An energy spectrum of tagged neutrons prior to a background subtraction is presented in Fig. 3.5. Specific neutron energies corresponding to the 38 ns and 96 ns bounds are calculated using Eq. 1.12 together with experimental values for $\Delta t_{\gamma\gamma}$ and $\Delta t_{n\gamma}$. Neutrons which deposit energies lower than 1 MeV do not exceed the detector threshold and thus do not appear in the data, while neutrons with energies higher than 6.6 MeV do not correlate with the 4.44 MeV signature gamma-ray emission from the de-excitation of $^{12}C^{*}$ and hence are not tagged. There are apparent peaks at $\sim$ 3 and $\sim$ 4.5 MeV. However, the highest number of counts occurs at energies below 2 MeV, which correspond mostly to background rather than tagged neutrons.

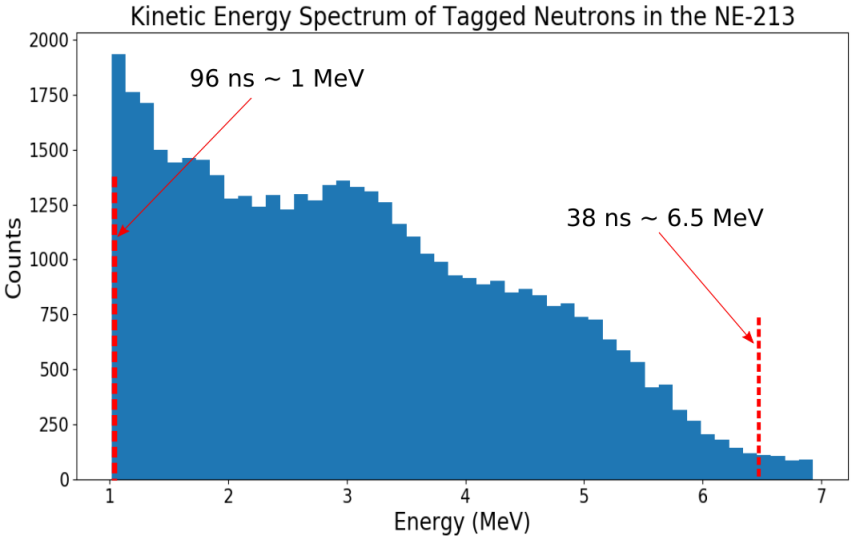

Figure 3.5: Energy spectrum without background correction. The red dashed line at 1 MeV corresponds to neutrons with a 96 ns flight time while the red dashed line at 6.6 MeV corresponds to neutrons with a 38 ns flight time. The bumps are caused by neutron counts while the shoulder structure with high counts between 1 and 2 MeV is composed mostly of background.

An estimated background subtraction of a factor of $1/T_n$ to the energy spectrum from Fig. 3.5 results in the plot presented in the left of Figure 3.6. This subtraction is an approximation. The dominant peak is now at 3.4 MeV with additional peaks of equal height at 2 and $\sim$ 4.5 MeV. Comparing the spectra with published results yields a better understanding of the general structure and peak positions.

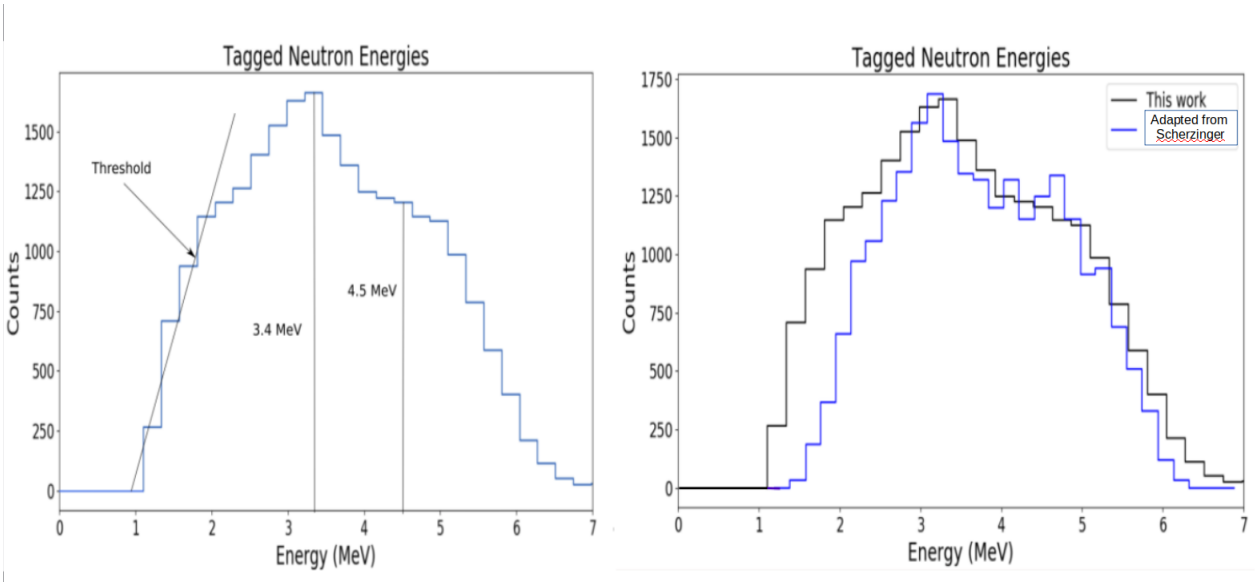

Figure 3.6: (Left) Energy spectrum with estimated background correction. The solid black lines at 3.4 and 4.5 MeV indicate energy peaks. The sloped line indicates the hardware threshold. (Right) The result adapted from [10] is shown in blue and the result from this work is shown in black.

The right plot on Figure 3.6 presents a comparison between the result in this work and the result published in [10]. While the structures share similarities, the spectrum in black is noticeably wider than the one in blue with significantly more counts at energies between 1 and 2 MeV. This implies the 24 mV hardware threshold used in this thesis is lower than that of [10]. The position of the black peak is shifted towards higher energies (3.4 MeV) compared to the one in blue ($\sim$ 3.2 MeV). Furthermore, the blue spectrum from [10] shows a distinct, second peak at $\sim$ 4.5 MeV while the black spectrum does not have a well-defined second peak.

The work from Scherzinger used a quasi-digital electronic configuration as opposed to the digital setup used in this work. The hardware threshold in the work of Scherzinger is given in electron volt equivalent as 200 keV_{ee} which corresponds to a neutron kinetic energy of $\approx$ 1 MeV [20].

Chapter 4 | Closing Remarks

4.1 Summary

A neutron ToF measurement was performed using an Actinide-Beryllium source and two scintillator detectors. A waveform digitizer was used for data acquisition. Neutron ToFs were measured with respect to gamma-ray coincidence events (the gamma-flash) in the scintillator detectors. The gamma-flash events served to calibrate the system. The gamma-ray coincidence events, $\Delta t_{\gamma\gamma}$, were measured with a flight time of (4.18 ± 0.06) ns. This value falls within the expected value of $\Delta t_{\gamma\gamma} = (4.16 \pm 0.01)$ ns based on the distance measurements for D and d. Neutrons with flight-times of up to 38 ns, corresponding with energies of ~ 6.6 MeV, were measured in agreement with expectations. A distinct peak in neutron energy counts at ~ 3.5 MeV was observed. However, due to the approximation for the background subtraction, it is difficult to properly compare the energy spectra produced in this work to those from published studies, particularly with regards to energies between 1 and 2 MeV and an expected, secondary peak at approximately 4.5 MeV.

4.2 Outlook

An immediate and necessary improvement for this work is to perform the background correction to the data. Once this issue is addressed, a more accurate comparison to previous results such as those from [10] and [15] may be possible. This work can be expanded further. An additional structure appears to the left of the gamma-flash in all ToF spectra shown so far. Since it also appears in Fig. 3.1, it is evidently not created by any of the analysis procedures but rather a part of the data itself. A suggestion on the nature of this bump is a neutron triggering the YAP detector and a gamma-ray triggering the NE-213. If so, studying this bump would be a way to characterize the neutron sensitivity of the YAP. Just like the $\Delta t_{\gamma n}$ times, this bump has an associated time range corresponding to the neutron energy range. Two additional expressions would be added to those in Eq. 1.7 - the time it takes for a neutron to reach the YAP, t', and the ToF of these neutrons Δt^*. These would be defined as

$$\begin{aligned} t' - t_0 &= \frac{d}{v_n} \\ \Delta t^* &= \Delta t_{\gamma\gamma} - t'. \end{aligned} \tag{4.1}$$

Since this bump is next to the gamma-flash, a sum of two Gaussian functions could be applied to approximate the center and width of both the bump and the gamma-flash. Alternatively, it may be that a Gaussian function is not the most accurate curve fitting procedure.

Bibliography

[1] Hughes, D. J. *Neutron Cross Sections* (Brook Haven National Laboratory, New York, 1958).

[2] Peggs, S. *et al.* ESS conceptual design report (2012).

[3] NIST, N. *Reference on Constants, Units and Uncertainty*

[4] Mauri, G. *et al.* Fast neutron sensitivity of neutron detectors based on Boron-10 converter layers. *Journal of Instrumentation* **13,** P03004–P03004. `https://doi.org/10.1088%2F1748-0221%2F13%2F03%2Fp03004` (2018).

[5] Knoll, G. F. *Radiation Detection and Measurement* (Wiley, New York, 1978).

[6] Lilley, J. *Nuclear Physics Principles and Applications* (Wiley, New York, 2001).

[7] Leo, W. *Techniques for Nuclear and Particle Physics Experiments* (Springer-Verlag, Berlin, 1987).

[8] Hassanabadi, H. & Hosseini, S. Branching ratios of -decay to ground and excited states of Fm, Cf, Cm and Pu. *Nuclear Physics A* **974,** 72–85. ISSN: 0375-9474. `http://www.sciencedirect.com/science/article/pii/S0375947418300587` (2018).

[9] Edward Anderson, M. & Bond, W. H. Neutron spectrum of a plutonium-beryllium source. *Nuclear Physics* **43,** 330–338. ISSN: 0029-5582. `http://www.sciencedirect.com/science/article/pii/0029558263903523` (1963).

[10] Scherzinger, J. *Neutron Irradiation Techniques* PhD thesis (Lund University, Lund, Skåne, 2016).

[11] Mauritszon, N. *Design, Construction, and Characterization of a Portable Neutron Detector* MA thesis (Lund University, Lund, Skåne, 2017).

[12] Technology, E. *Neutron/Gamma PSD EJ-301*

[13] Baccaro, S. *et al.* Scintillation properties of YAP:Ce. *Nuclear Instruments Methods in Physics Research Section A-accelerators Spectrometers Detectors and Associated Equipment - NUCL INSTRUM METH PHYS RES A* **361,** 209–215 (1995).

[14] CAEN. *User Manual, UM3350, V1751/VX1751, 4/8 Channels 10 bit 2/2 GS/s Digitizer* (2017).

[15] Kjaer, R. H. *Identifications of Neutrons Using Digitized Waveforms* MA thesis (Lund University, Lund, Skåne, 2019).

[16] Anonymous. *Constant Fraction 1.svg* 2006.

[17] Messi, F. *et al.* The neutron tagging facility at Lund University. *arXiv preprint arXiv:1711.10286* (2017).

[18] CAEN. *User Manual, UM6009, 751 Family Waveform Recording Firmware Registers* (2017).

[19] Pandas development team, T. *pandas-dev/pandas: Pandas* version latest. 2020. https://doi.org/10.5281/zenodo.3509134.

[20] Scherzinger, J. *et al.* A comparison of untagged gamma-ray and tagged-neutron yields from 241AmBe and 238PuBe sources. *Applied Radiation and Isotopes* **127,** 98–102 (2017).